OMAE2019-95920

MECHANICAL MODELING OF THE POLYMERIC COATING ON A SUBSEA PIPELINE

Ole Vestrum[*]
Magnus Langseth
Tore Børvik
Structural Impact Laboratory (SIMLab)
Centre for Research-based Innovation (CRI)
Department of Structural Engineering
Norwegian University of Science and Technology
Rich. Birkelands vei 1, NO-7491 Trondheim, Norway
E-mail: ole.vestrum@ntnu.no

ABSTRACT

Offshore pipelines may be exposed to a range of extreme loading situations during operation on the seabed such as impact by trawl gear or anchors. While not primarily being designed for it, thermal insulating polymeric coatings are experienced to provide beneficial contributions to the structural integrity of subsea pipeline designs. In recent editions, the prevailing standards and design guidelines are allowing for the inclusion of external coating products in the mechanical design evaluation. This secondary functionality of insulating coatings presents a great potential in terms of more optimized pipeline designs. However, due to the lack of reliable and versatile mechanical models, any beneficial effects from these complex polymeric insulating coatings are often omitted in simulations. This work presents a finite element based approach for assessing the mechanical response of polymeric coatings on offshore pipelines with different porous structures imaged using X-ray micro computed tomography. The modeling approach is also compared with experimental results.

INTRODUCTION

Rigid steel pipelines are used to convey oil and gas along the seafloor by the offshore industry. The high inherent temperatures and pressures drive the fluids topside from the reser-voirs. Therefore, pipelines are insulated with thick polymeric coating solutions in order to prevent loss of heat. While often installed without any dedicated mechanical protective measures (trenching, covers, armors, etc), the long-spanning components are rendered vulnerable to extreme loading situations. Extreme loading situations may be caused by impact from moving objects like fish trawling gear or falling anchors [1]. Vestrum et al. [2] proved significant energy absorbing capabilities of a polymeric insulating coating during impact from moving objects. As both pipelines network systems and cross-section architectures are designed with respect to the likelihood and risks of such accidental events [3], a great economical potential exists in the inclusion of the thermal insulation during mechanical assessments. However, due to their complex material and design features, any beneficial effects introduced by the presence of polymeric insulating coatings are often omitted in mechanical design evaluations. Prevailing standards and design guidelines are allowing for thermal coatings to be included however, their effectiveness must be documented [3, 4]. This may be done with full-scale component-specific experiments [5, 6]. However, a cost-effective alternative to expensive experimental programs are found in numerical techniques as the finite element method. For such tools to be accurate and versatile, efforts need to be made towards developing good modeling strategies. As many pipeline coating products consist of multiple layers with unique and complex characteristics, conventional finite element models may not suffice in accurately de-

---

[*]Corresponding author
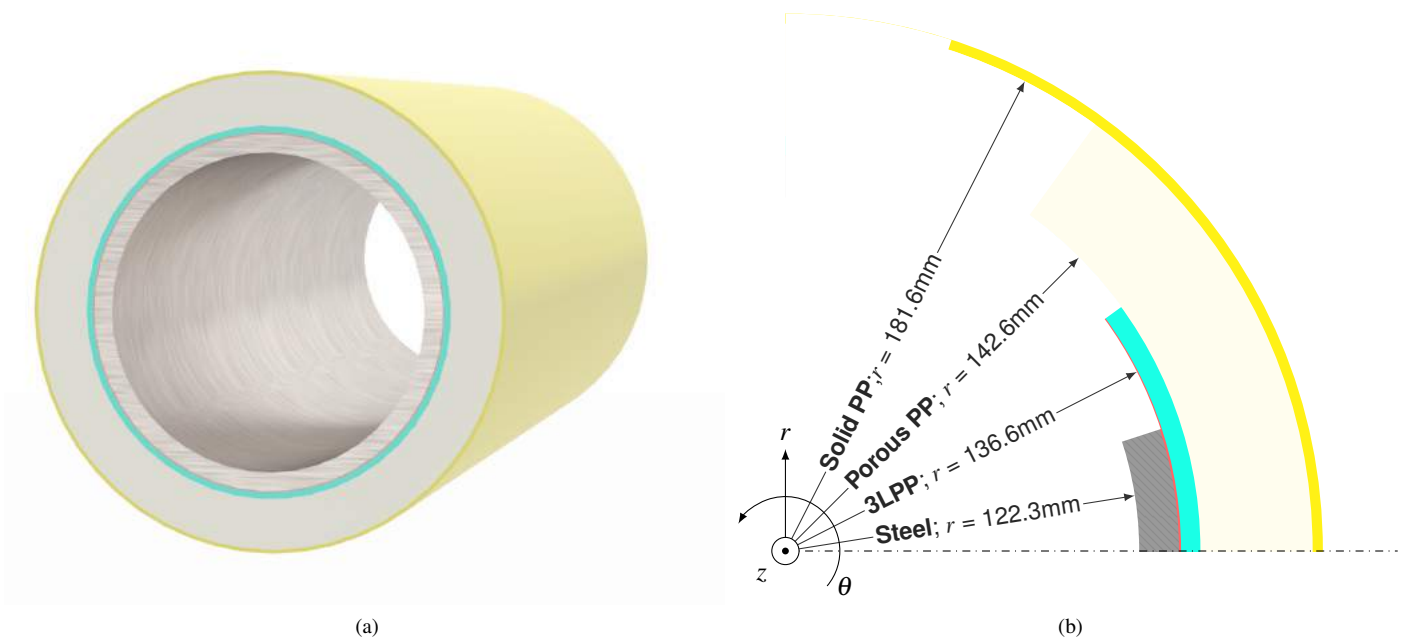
FIGURE 1: Illustrations of the particular coated pipeline design studied in this work.

scribing their combined response for advanced engineering purposes.

In this work, an alternative modeling approach for assessing the mechanical response of insulating pipeline coatings is presented. The approach employs X-ray micro computed tomography in mapping the porous structure of the insulation layers. These mappings are used to derive finite element models representing the exact macroscopic morphology. Actual specimens from a typical polymeric insulation coating are modeled using the presented approach, while the same specimens were also experimentally tested in uniaxial compression. The experiments were used to validate the modeling approach. It is concluded that the modeling approach managed to adequately capture the mechanical behavior at low deformations (though well into the post-yield domain) produced by the specimens with very different porous morphologies. While improvements are suggested for the model, the current approach may serve as a reasonable lower-bound estimate for the compressive behavior of similar coatings.

MATERIAL

The insulating coating solution used to exemplify the mechanical modeling approach herein is a multilayer polypropylene system produced by Shawcor Norway under the product name Thermotite [7]. The layering structure is customizable and a certain coating design depends on the operational demands of the pipeline. While the majority of a full coating volume consist of a thermal insulating layer, other thinner layers are also included in the system. These are applied to shield the pipeline from a corrosive and generally harsh ambient environment. Figure 1(a) gives an illustration of the steel pipeline with the particular multilayer design used in the work presented herein. Figure 1(b) presents a portion of a cross-section with the study-specific layering scheme where a 3-layer polypropylene (3LPP, 6mm thick) system was applied to an X65 pipeline, followed by a thick layer of foamed polypropylene (Porous PP, 39mm thick) and an outer layer of solid polypropylene (Solid PP, 3mm thick). The 3LPP layer is an integrated solution providing corrosion protection for the steel and adhesion to the insulating coating, the Porous PP layer insulates the pipeline preventing heat loss in multiphase flow, while the external Solid PP serves as a shield for the inner layers of the cross-section. Coating specimens were retrieved from virgin pipeline samples from a production batch intended for operational use. Other pipeline samples from the same batch have previously been studied in terms of the coating products ability to absorb energy during impact events [2, 6]. Previous studies [5] revealed a strong variation in the porous morphology throughout the thickness of the Porous PP with possible implications for the mechanical response (and thus energy absorption) of the full coating. It is these implications that are further examined herein. To this end, five cylindrical specimens throughout the Porous PP layer were sampled and further studied. Figure 2 gives the positions and corresponding labels (A to E) indicating where the specimens were retrieved across the layer thickness.
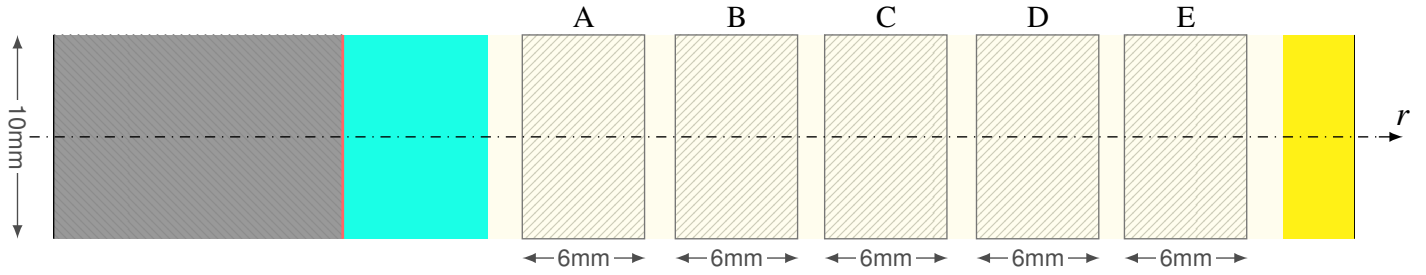
FIGURE 2: Overview of the original positions and corresponding labels of the cylindrical coating specimens retrieved. See Figure 1(b) for the cross-section related to the layer measures.

All specimens were cylinders with axes of symmetry parallel to r (see Figure 1(b)) and with nominal heights and diameters of 6mm and 10mm, respectively.

## X-RAY MICRO COMPUTED TOMOGRAPHY

X-ray micro computed tomography (XRMCT) is a general and nondestructive testing method using a series of two-dimensional X-ray projections (radiographs) to reconstruct a three-dimensional image of the densities in a body. X-ray radiation is passed through the specimen where it is attenuated. As the solid polypropylene attenuates much more radiation than the vacant pores, high resolute mappings of the two-phased structure is possible. The pore morphologies of the five cylindrical specimens were mapped using XRMCT. All scans were conducted at facilities located at the Norwegian University of Science and Technology (NTNU) in Trondheim using a Nikon XT H225 ST MicroCT machine. The reconstructions of the three-dimensional density images were made with the commercial software Nikon CT Pro 3D (Version XT 3.1.3).

Figure 3 presents rendered surface models created from the raw data of the XRMCT scans. It is readily seen that the morphology differs between the specimens. Previous work [2] revealed a concave variation in terms of density across the layer thickness. This may also visually be deduced from the porosities seen across the specimens in the figure: Specimen C is readily seen to be more porous than the specimens A and E sampled closed to the layer boundaries.
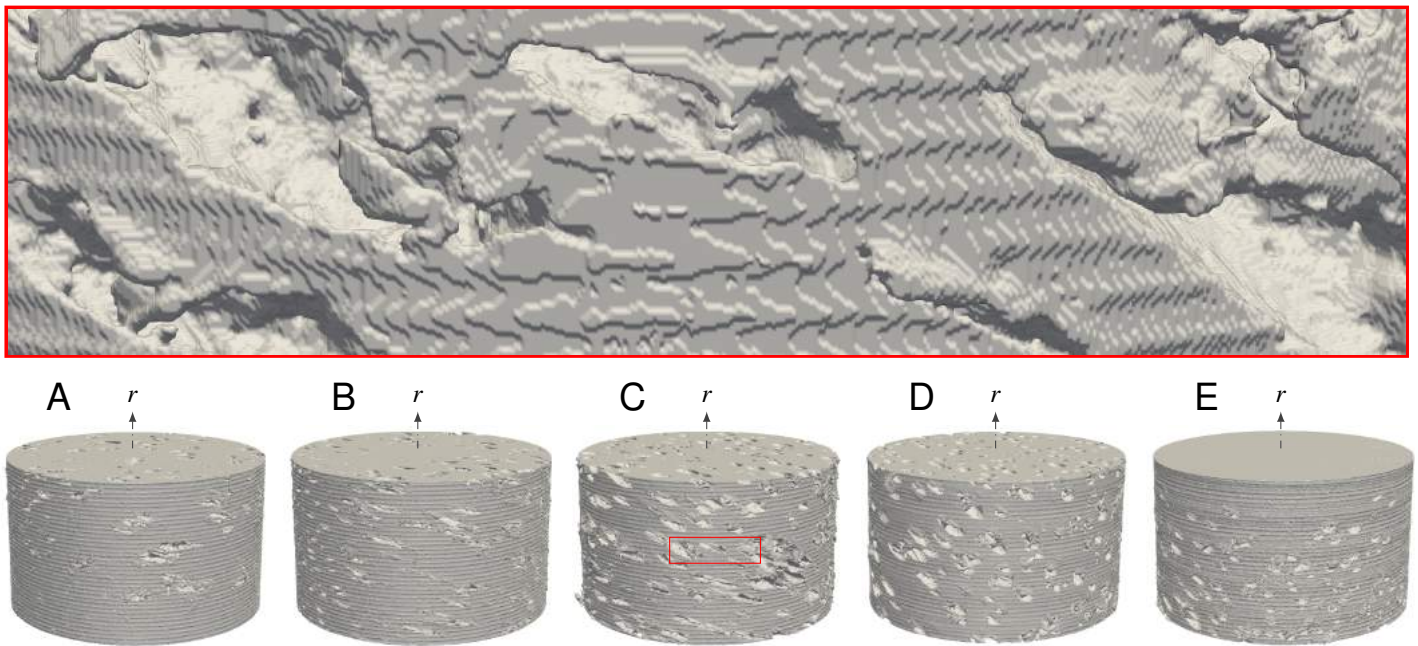
**FIGURE 3**: Surface models from the XRMCT of the five specimens with a close-up of specimen C.
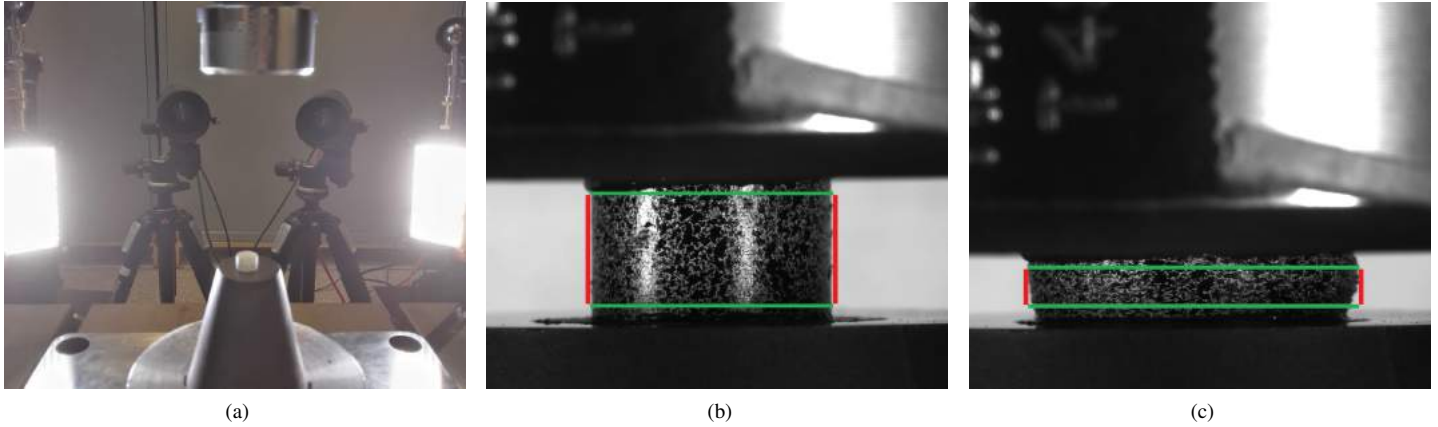
FIGURE 4: Images from (a) the test setup, and recorded deformation images at (b) 0.0mm and (c) 3.0mm of specimen A.

MECHANICAL TESTS

Following the XRMCT, all specimens were tested in uniaxial compression in order to map their mechanical response. The tests were performed using an Instron 5982-L2035 [8] universal test machine at a deformation rate of 0.006mm/s. Multipurpose lubrication was applied to both the top and bottom of the cylindrical specimens to minimize friction at the interfaces. The reaction forces (F) were recorded using an Instron 2580-301 (100kN) load cell with a $\pm 0.15\%$ measuring error within the force ranges achieved during testing. Figure 4(a) shows the test setup with the specimen placed in the testing machine in the foreground and two

5-megapixel Prosilica GC2450 cameras in the background (only one of these was used in the post-processing presented herein). The cameras were used to take still images of the specimens during deformation. Figure 4(b) and (c) provides two images at 0.0mm and 3.0mm of deformation, respectively. The peripheral edges of the deforming geometries were traced (using self-written software routines in Python). These tracings were used to estimate the updated cross-section areas (A) of the specimens during deformation. The results from this edge tracing are visualized as vertical red lines in Figure 4(b) and (c). From these
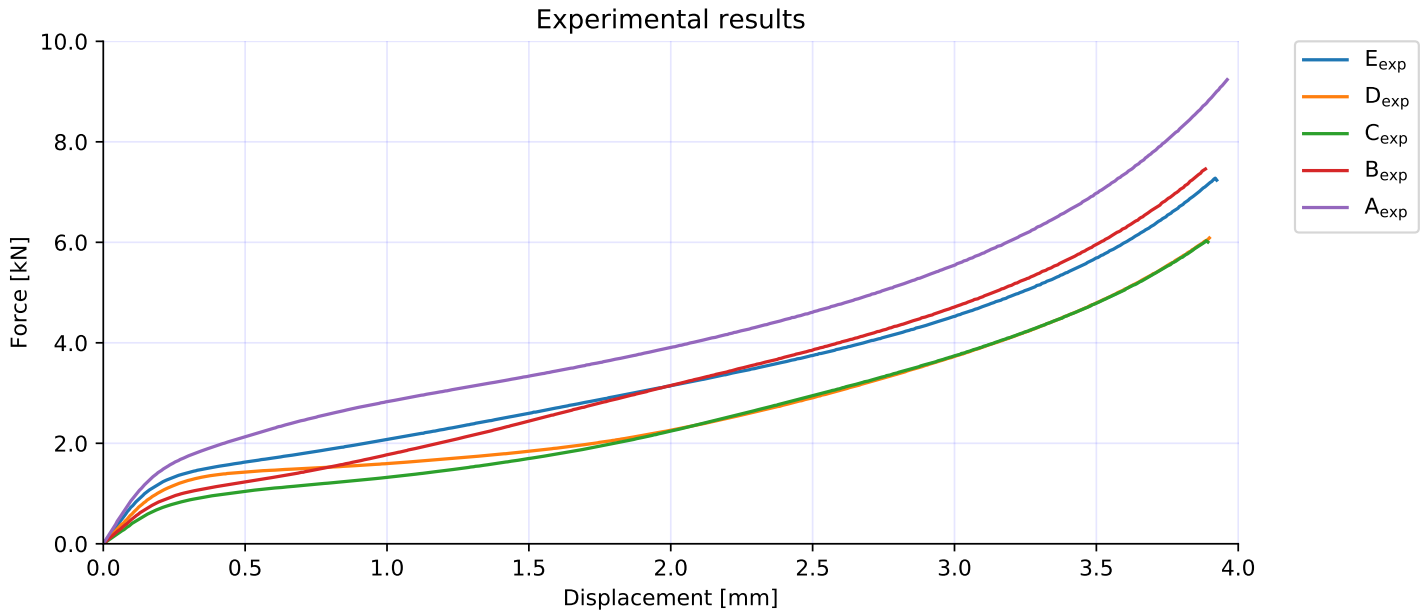
FIGURE 5: Force-displacement curves from uniaxial compression of the porous specimens.
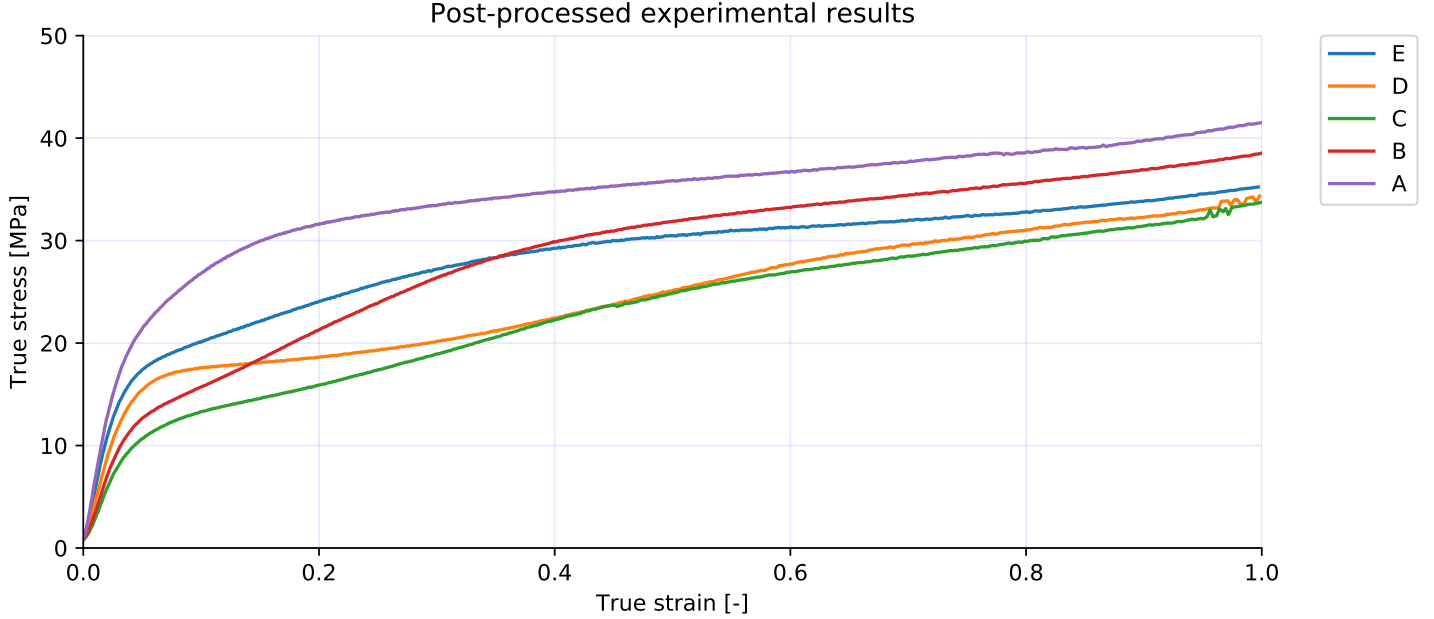
FIGURE 6: True stress-strain curves derived with Equation 1 and 2 from results given in Figure 5.

measures, the true stress (σ) could be estimated via

$$\sigma = F/A. \tag{1}$$

The crosshead displacement (Δ) was deemed as an adequate measure for this study as the error at the maximum force achieved was measured to be less than 2%. Provided the height of the specimen (h), the true strain could be calculated through the relation

$$\varepsilon = \ln\left(1 + \Delta/h\right). \tag{2}$$

Both the air humidity and temperature were measured during the testing period and found to be in the intervals of 26-28% and 22-25°C, respectively.

Figure 5 presents force-displacement curves from the tests using the described setup. Clear differences are seen between the specimens in terms of uniaxial compressive behavior. While having similar initial responses, specimens B and C are seen to diverge early on during deformation with B converging to E at larger deformations. Similar behavior is seen between specimens D and E with comparable pre-yield response, with D converging with C (crossing paths with B at around 0.75mm) at larger deformation.

The force-displacement curves in Figure 5 were used in the calculation of the true stress-strain curves shown in Figure 6.

There exist contradictions in deriving material data from such highly inhomogenous specimens. Due to the graded porosity across the specimen height, the strains tend to localize in the less dense regions. This may be thought to occur due to the increased stress across the least dense regions, having the lowest cross-sectional area. It will therefore exists a stress distribution throughout the specimen height. While the presented compression tests may not necessarily be strictly usable as material characterization tests, they are indeed viable component tests that can be used to evaluate the model approach presented herein.

IMAGE-BASED MODELING

The rendered surface models in Figure 3 are heavily post-processed and are not the starting point of the modeling approach derived in this section. The actual raw data from the XRMCT may be thought of as a three-dimensional array (image) of gray-scale values with range {0, 255} (where an increasing value corresponds to increasing material density) and domain 2000×2000×2000. Each element in the three-dimensional array is called a voxel (analogous to a pixel in a two-dimensional image). The spatial resolution of voxels will vary between individual XRMCT scans, but sub 0.01mm-resolution was achieved for the scans presented herein. The raw XRMCT data set holds 8.0e9 (2000^3) values between 0 and 255 representing the relative X-ray attenuation (i.e., radiodensity) across the scanned volume.

Voxel-based finite element models have been used in earlier studies of cellular materials [9], and presents an efficient
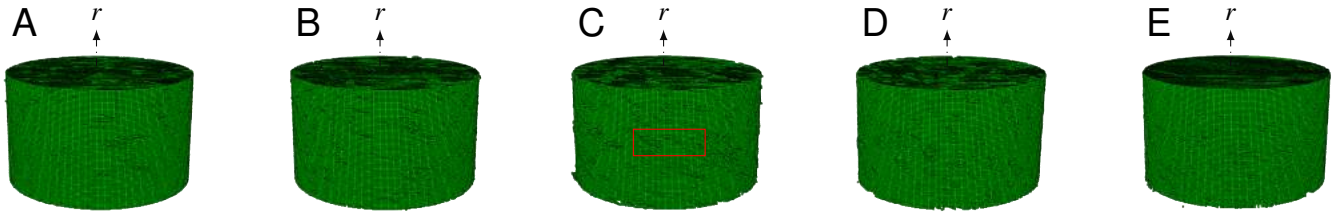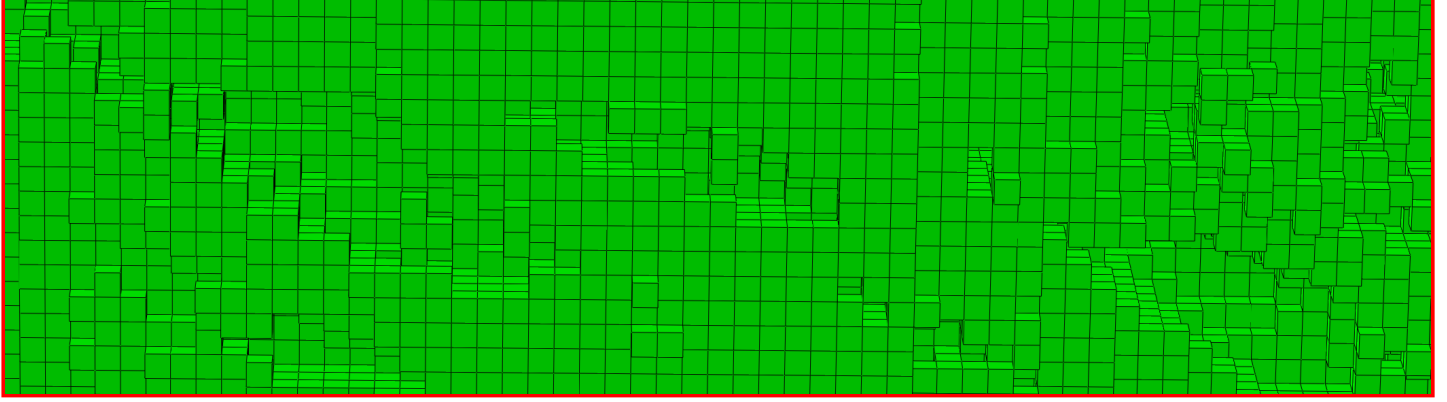
FIGURE 7: Undeformed meshes produced from the XRMCT mappings (with a close-up of specimen C) using the stepwise rutine outlined below.

and pragmatic approach of integrating XRMCT data into finite element analysis by replacing the voxels-based data sets with meshes of hexagonal elements. The modeling approach presented herein is derived on this idea. All the model meshes were created using self-developed Python software routines. This makes the solution method a cost-efficient alternative compared to a more advanced tetrahedral-based meshing which needs more sophisticated and costly commercial software. A more detailed derivation of the applied approach is given by Vestrum et al. [10], while a conceptual overview is presented in the following:

1. Mapping the densities in the sample via XRMCT resulting in a three-dimensional array of gray level values denoted $\boldsymbol{\omega}$. Adopting index notation, the elements in the XRMCT data set may be expressed as

$$\omega_{ijk} \in \{0,1,2,...,253,254,255\}^{m\times n\times o} \quad (3)$$

where m = n = o = 2000.

2. As the XRMCT data is prone to noise (i.e., high frequency local fluctuations in ω_{ijk}), $\boldsymbol{\omega}$ needs to be low-pass filtered to facilitate subsequent steps. The filtering is more precisely expressed as the convolution between $\boldsymbol{\omega}$ and a suitable filter kernel $\boldsymbol{g}$ – and the filtered data set is formulated as

$$\tilde{\boldsymbol{\omega}} = \boldsymbol{\omega} * \boldsymbol{g} \quad (4)$$

so that $\tilde{\omega}_{ijk} \in \{0,1,2,...,253,254,255\}^{m\times n\times o}$.

3. As the final goal of this process is to convert the density mapping into finite elements, a domain of 8.0e9 would yield a mesh containing far too many elements to be processed. Thus, a reduction of the domain is necessary. A downscaling of the resolution of $\tilde{\boldsymbol{\omega}}$ is denoted in index form as

$$\check{\omega}_{ijk} \in \{0,1,2,...,253,254,255\}^{a\times b\times c} \quad (5)$$

with $a = b = c = x$. The value of x will govern the element size and has to be chosen with respect to both the computational efficiency and accuracy of the model.

4. The next step is to separate matter from void (or foreground from background). This separation of distinct phases is known as segmentation in the field of image processing. As the two phases manifest themselves as two distinct peaks within the full gray-scale spectrum of $\check{\boldsymbol{\omega}}$, a single threshold value may be used to distinguish them. This is known as binarization. There are various approaches, with various degrees of sophistication, in how to establish a suitable gray level threshold. The most simplistic approach would be to plot the gray-scale histogram of $\check{\boldsymbol{\omega}}$, and simply identifying a threshold value, which separates the two peaks. In this binarization operation, all gray levels above the threshold value is identified as matter (foreground / white / 1) while all levels below is considered to be void (background / black / 0).
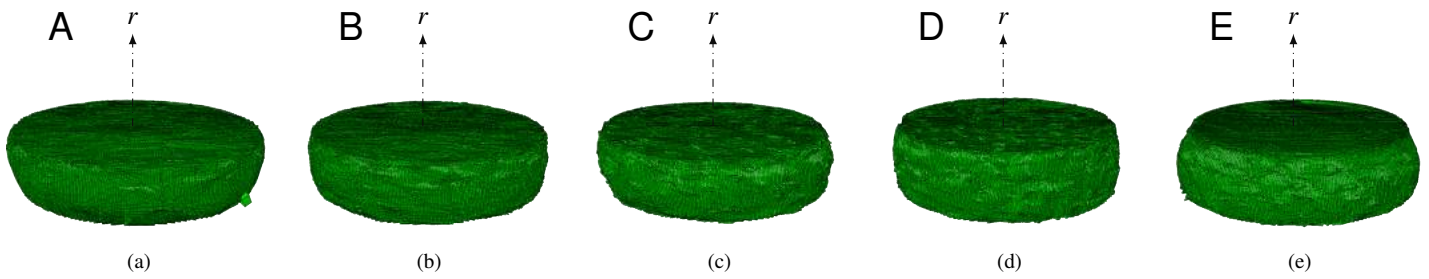
6

FIGURE 8: Deformed configurations at around 3.0mm displacement.

The resulting data set is expressed as

$$\bar{\omega}_{ijk} = \{0,1\}^{a \times b \times c}. \tag{6}$$

5. The final step is to port $\bar{\boldsymbol{\omega}}$ to a chosen finite element solver. In this work, Abaqus/Explicit (hereby Abaqus) has been applied. Each entry of $\bar{\boldsymbol{\omega}}$ is converted into an element in a part
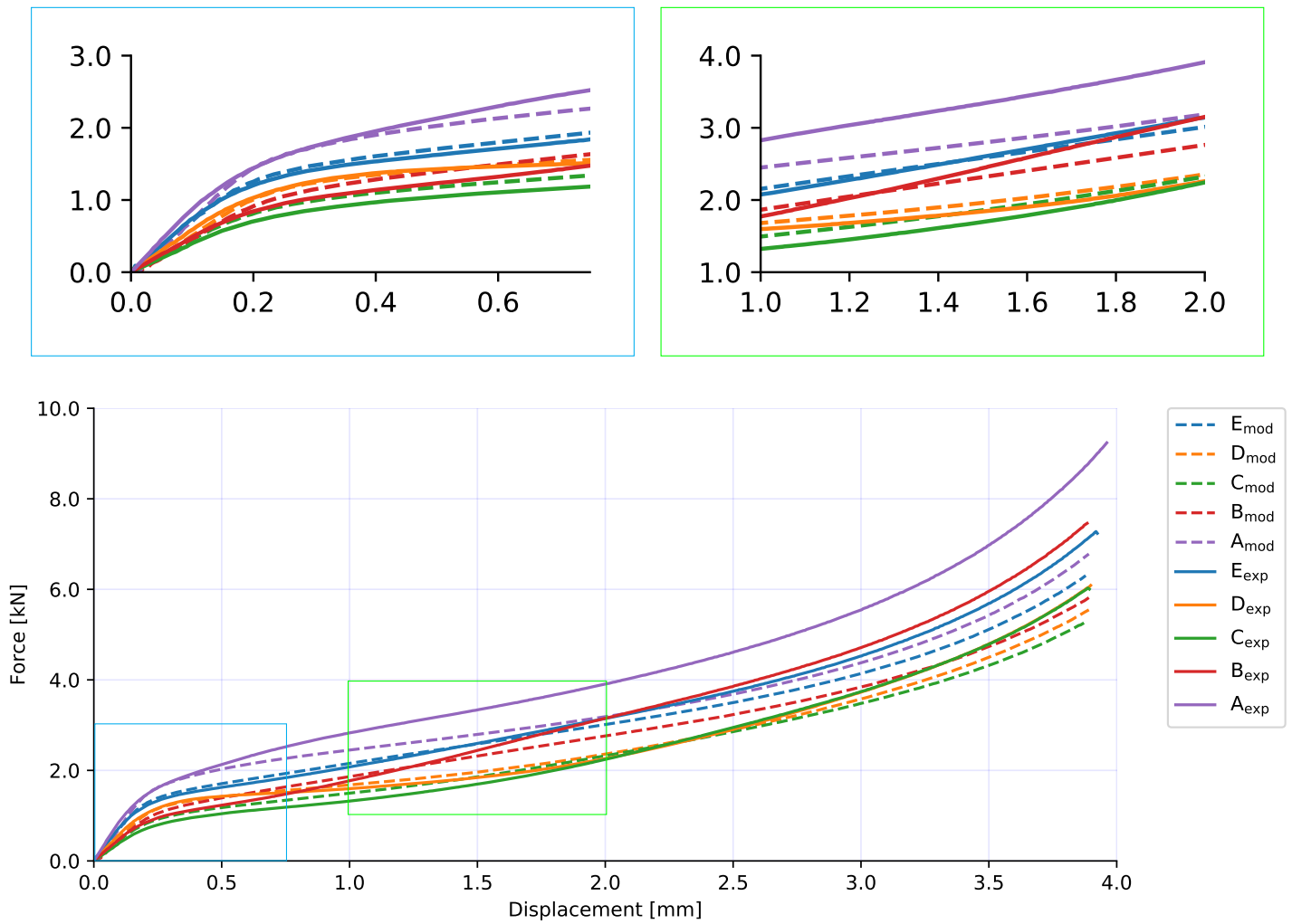

FIGURE 9: Comparison between experimental (solid lines) and model (dashed lines) force-displacement curve.

mesh. This is done by establishing node, element and connectivity tables exported to input files readable by Abaqus.

The meshes seen in Figure 7 were produced via the outlined procedure and these are used in the full model setups of the compression experiments. Two analytical rigid surfaces are placed at the top and bottom of each cylindrical specimen in the FE-model, representing the interface to the testing machine. A velocity is smoothly imposed to the top surface using a general contact formulation (with minor friction) between both surfaces and specimen. The velocity (which was chosen to yield quasi-static conditions) resulted in a displacement of the surface, which in turn compressed the specimen due to the contact properties. A second contact definition is added to account for the self-contact within the specimen itself. The reaction forces and displacements are recorded in the top surface for comparison with the experimental results.

The matrix material of the porous layer was made from a polypropylene material produced by Borealis under the product name BA202E. The data sheet of BA202E [11] indicates an initial yield stress in tension at 28MPa (σ_0) with a mass density of 900kg/m^3. A reasonable run time for the models (around 16 hours at an in-house computational cluster) was found with x corresponding to an element size of 0.08mm. Along with an elastic modulus (E) of 800MPa, the material parameters constituted the input for a linear elastic J$_2$ plasticity model with no work hardening used with the developed meshes. The equivalent stress (σ) in terms of the equivalent strain (ε) applied in the model is formulated as

$$\sigma(\varepsilon) = \begin{cases} E\varepsilon & \text{if} \quad \varepsilon < \sigma_0/E \\ \sigma_0 & \text{if} \quad \varepsilon \geq \sigma_0/E \end{cases} \quad (7)$$

Figure 8 presents deformed configurations of the undeformed meshes in Figure 7 at displacements of 3.0mm. The respective deformed configurations are readily seen to vary among the specimens at this displacement. When comparing Figure 8 (a) to that of Figure 4(c), comparable curvatures of the pheriphical sides are seen. By studying specimen A and E in Figure 3, one can see that the top of the specimen is observably more porous for A, while the same goes from the bottom of specimen E. In Figure 8 it may be seen that these regions experience a larger radial (cylindrical radius, and not r in Figure 1(b)) expansion than at the opposing ends. This may be caused by less constrained deformations in these relatively low-density parts.

In Figure 9, the force-displacement curves produced by the described model (dashed lines) have been plotted alongside the experimental results (solid lines). While only differing in terms of specimen geometries (i.e., the same material definition for the matrix material across the specimens), the global yield points are seen to be reproduced well. The force levels produced by

the model shows excellent correspondence at lower levels of deformations ($\Delta < 0.75$). However, neither the exponential force-increase nor the cross-over characteristics of the graphs observed in the experiments (as commented upon previously) are replicated with the proposed model.

CONCLUSION

The presented modeling approach is seen to provide a reliable lower-bound estimate for the mechanical response of polymeric coating in compression. This is achieved using only the XRMCT data, mapping the pore morphology into a FE-model, and readily available material data from the data sheet of the matrix material. At larger deformations, the models do not experience the characteristic evolutions in terms of force-versus-displacement as in the corresponding experiments. This may be caused by an over-simplistic mechanical representation of the polymeric matrix in the finite elements, which is suggested for future work.

REFERENCES

[1] The Petroleum Safety Authority Norway, 2017. *Rorledningsskader Skader og hendelser fra Petroleumstilsynet CODAM database.* http://www.psa.no/getfile.php/1345620/PDF/Roerledningsskader%20Oktober2017.pdf. Online: Accessed 28-December-2018.

[2] Vestrum, O., Kristoffersen, M., Polanco-Loria, M. A., Ilstad, H., Langseth, M., and Børvik, T., 2018. "Quasi-static and dynamic indentation of offshore pipelines with and without multi-layer polymeric coating". *Marine Structures, Volume 62*, pp. 60–75.

[3] DNV, 2013. *DNV-OS-F101 Submarine Pipeline Systems*, October. Offshore Standard.

[4] DNVGL, 2017. *DNVGL-RP-111 Interference between trawl gear and pipelines*, May. Recommended practice.

[5] Vestrum, O., Kristoffersen, M., Polanco-Loria, M. A., Ilstad, H., Langseth, M., and Børvik, T., 2017. "Quasi-Static and Dynamic Deformation of Polymer Coated Pipes". *ASME 2017 36th International Conference on Ocean, Offshore and Arctic Engineering, Volume 3A*. OMAE2017-62506.

[6] Polanco-Loria, M. A., Ilstad, H., and Levold, E., 2017. "A Numerical-Experimental Approach of Indentation Problem: Part II - Force-Dent Response of Polymeric Coated Steel Pipes". *ASME 2017 36th International Conference on Ocean, Offshore and Arctic Engineering,* **Volume 5B**. OMAE2017-61902.

[7] SHAWCOR, 2018. *Thermotite (Polypropylene Foam).* https://www.shawcor.com/pipe-coating-solutions/products/thermotite-(polypropylene-foam). Online: Accessed 28-December-2018.

[8] INSTRON, 2018. *5980 Floor Model Systems for High-Capacity Universal Testing*. Online: Accessed 22-December-2018.

[9] Buffière, J. Y., Cloetens, P., Ludwig, W., Maire, E., and Salvo, L., 2008. "In Situ X-Ray Tomography Studies of Microstructural Evolution Combined with 3D Modeling. Three-Dimensional Materials Science". *Three-Dimensional Materials Science,* **Volume 33**.

[10] Vestrum, O., Langseth, M., and Børvik, T., 2019. "Finite element modeling of porous polymer pipeline coating using X-ray micro computed tomography". *Submitted for possible journal publication*.

[11] BOREALIS, 2018. *Borealis BA202E.* https://www.borealisgroup.com/storage/Datasheets/ba202e/ BA202E-PDS-REG_EUROPE-EN-V8-PDS-EUR-24472-10048594.pdf. Online; accessed 13-December-2018.